Theoretical study on proton diffusivity in Y-doped $BaZrO_3$ with realistic dopant configurations

Takeo Fujii[1], Kazuaki Toyoura[*,1], Tetsuya Uda[1], and Shusuke Kasamatsu[**,2]

[1] *Department of Materials Science and Engineering, Kyoto University, Kyoto 606-8501, Japan*

[2] *Academic Assembly (Faculty of Science), Yamagata University, Yamagata 990-8560, Japan*

* toyoura.kazuaki.5r@kyoto-u.ac.jp

** kasamatsu@sci.kj.yamagata-u.ac.jp

Abstract

We theoretically revisit the proton diffusivity in yttrium-doped barium zirconate (Y-doped $BaZrO_3$) with realistic dopant configurations under processing conditions. In a recent study employing the replica exchange Monte Carlo method, the equilibrium Y configurations at typical sintering temperatures were shown to deviate from the random configuration assumed in earlier theoretical studies. In the present study, we took this observation into account and evaluated the effect of the Y configuration on the proton diffusivity. Using the master equation approach based on local diffusion barriers calculated from first principles, the proton diffusivities under realistic Y configurations were estimated to be higher than those in the random configuration. This is explained by the fact that realistic Y configurations have fewer trap sites with deep potential wells compared to the random configuration due to the isolation trend of Y dopants. In addition, the effects of proton-proton interaction and the abundance of preferential conduction pathways are discussed; it is found that both are relatively minor factors compared to the trap site effect in determining the dependence of the proton diffusivity on the Y configurations.

1. Introduction

Acceptor-doped barium zirconate ($BaZrO_3$) with the cubic perovskite structure has both high proton conductivity and high chemical stability [1-5], which makes it a promising candidate for electrolytes in various electrochemical devices such as fuel cells and electrolyzers. Yttrium ions (Y^{3+} ions) are typical dopant species for $BaZrO_3$ [6-8], substituting Zr^{4+} sites to introduce protons into the crystal by the charge compensation mechanism. The proton conductivity depends on the Y dopant concentration x_Y with a maximum at $x_Y \sim 0.2$, where x_Y is defined as the occupancy of Y dopants on Zr sites, i.e., $BaZr_{1-x_Y}Y_{x_Y}O_{3-\delta}$ [8].

The atomic-scale picture of the proton conduction mechanism in acceptor-doped $BaZrO_3$ has been investigated intensively [9-15]. According to experimental reports by nuclear magnetic resonance and infrared spectroscopies (IR, NMR) [9,10] and theoretical reports by first-principles calculations [11-15], protons mainly reside around oxide ions in the crystal to form an OH bond. They migrate over a long range through rotation around single oxide ions (reorientation of the OH bond) and hopping between adjacent oxide ions. The calculated potential barriers ΔE^{mig} of the proton rotation and hopping in the dopant-free crystal are mostly reported to be in the range of 0.1–0.2 eV and 0.2–0.3 eV, respectively [13-16], although a higher potential barrier for proton hopping (0.41 eV) has been reported recently [17]. In any case, proton hopping has a higher potential barrier than proton rotation in this system, meaning that the rate-determining step is the proton hopping in the case of negligible dopant-proton interaction.

The interaction between Y dopants and protons (Y-H interaction) is, however, a key factor governing the proton conductivity in Y-doped $BaZrO_3$. The negative formal charge of Y dopants on Zr sites stabilizes protons due to electrostatic attraction, leading to reduced proton diffusivity. This effect is called *proton trapping* in general. Yamazaki et al. extracted the proton migration energy, E_a, and the association energy between protons and Y dopants, E_{as}, from the temperature dependence of the proton diffusivity by simply assuming two types of protons in the crystal, i.e., free and trapped protons [18]. The reported E_a and E_{as} are 16 kJ/mol (0.17 eV) and 29 kJ/mol (0.30 eV) in $BaZr_{0.8}Y_{0.2}O_{3-\delta}$, respectively.

The above simple assumption is a good approximation for dilute-dopant systems, e.g., $x_Y \leq 0.01$, but the interaction between dopants and protons should be more complicated in highly doped systems. Toyoura et al. theoretically clarified the detailed interaction between Y dopants and protons by evaluating the potential barriers of proton rotation and hopping under various local Y configurations using first-principles calculations [19]. The calculated potential barriers were found to vary significantly depending on the local Y configuration, ranging from 0.08 eV to 1.08 eV for proton rotation and from 0.02 eV to 0.56 eV for proton hopping. They also performed diffusion simulations using the kinetic Monte Carlo (KMC) method based on the calculated barriers and found that trapping is quite strong at proton sites surrounded by three Y dopants. The number of such sites increases with dopant concentration x_Y in the $BaZrO_3$ crystal, leading to lower proton diffusivity. In addition, Toyoura et al. clarified that protons in highly doped $BaZrO_3$, e.g., $x_Y \sim 0.2$, preferentially migrate along the

three-dimensional (3D) network of Y dopants. The preferential proton conduction partially cancels the strong trapping effect of densely populated dopants, resulting in a minor reduction of the proton diffusivity in highly doped $BaZrO_3$. Draber et al. also reported the importance of Y connection by proposing a novel picture of proton diffusion mechanism, *nanoscale percolation* [17]. According to their calculations, protons migrate much faster in the trap region than in the trap-free region, leading to higher proton diffusivity at higher dopant concentration due to the more developed local connection of Y dopants. In their computational model, however, the potential energies of proton sites were assumed to have only two values corresponding to the trap and trap-free regions (to be more precise, they also considered repulsion between protons bonded to the same oxide ion, but the repulsion is so large that such states are seldom realized). This assumption leads to underestimation of the proton trapping effect at proton sites surrounded by multiple Y dopants, which can be one of reasons for the opposite dependence of proton diffusivity on the Y concentration to that in Ref. [19].

As for Y configurations on Zr sites in $BaZr_{1-x_Y}Y_{x_Y}O_{3-\delta}$, Y dopants are assumed to be randomly distributed in the above studies [17-19]. This simple assumption is only based on the high sintering temperature of $BaZrO_3$ above 1873 K. In addition, supercells with random distribution of Y-Y pairs were also employed in one of the previous reports [19]; this model was employed to examine the extreme case where all Y dopants exist in nearest-neighbor pairs, since the formation of Y-V_O-Y defect associates was reported to be energetically favorable in Ref. [20]. On the other hand, Kasamatsu et al. have recently reported the thermal equilibrium configurations of Y dopants and O vacancies in the

wide temperature range (600–2500 K), which were determined by a first-principles thermodynamic sampling simulation based on the replica exchange Monte Carlo (RXMC) method [21]. They claimed that the Y configuration in Y-doped $BaZrO_3$ does not reach the random configuration even at the highest temperature, suggesting that the above assumption concerning the Y configuration in the crystal could be too simple.

In the present study, we revisit, from first principles, the proton diffusivity in Y-doped $BaZrO_3$ focusing on the effect of Y configurations. Specifically, we estimate the proton diffusivities in multiple supercells reflecting the Y configuration in thermal equilibrium at the sintering temperature. The effect of the deviation from the random Y configuration on the proton diffusivity is discussed by focusing on local Y configurations around individual proton sites. The effect of proton-proton (H-H) interaction [17,22], which tends to slightly increase the proton diffusivity by the *trap-site filling* effect in this system [22], is additionally taken into consideration.

2. Computational methodology

2.1 Y configurations

As noted above, RXMC sampling of Y dopants on Zr sites and O vacancies configurations were performed in Ref. [21] by one of the authors. The sampling was performed within a 3×3×3 cubic perovskite supercell at varying Y concentrations (x_Y = 0.07, 0.15, 0.22, 0.30) and at 16 temperatures between T = 600 K and T = 2500 K. The calculations were repeated twice resulting in two independent equilibrium ensembles of 1400 configurations for each (x_Y, T) pair. It should be noted that the 3×3×3

supercells do not allow for consideration of Y agglomeration beyond pairs at $x_Y = 0.07$, because the low concentration corresponds to the 3×3×3 supercell with only two Y ions.

In principle, we can perform proton diffusivity calculations while keeping the Y positions fixed on each of the 1400 × 2 Y configurations at given (x_Y, T); the results may then be averaged to obtain the proton diffusivity vs. (x_Y, T), where T can be considered the sintering temperature which determines the Y configuration (to emphasize this point, we will denote the processing temperature as T_{sinter} hereafter). However, we found significant finite size effects when performing diffusivity calculations using the master equation approach (Sec. 2.2) in the 3×3×3 supercell. Thus, we decided to generate 9×9×9 supercell models designed to incorporate the cation-cation correlations of all 1400 configurations in each (x_Y, T_{sinter}) ensemble. To achieve this, we borrowed the idea from the generation of *special quasirandom structures* (SQS) [23], which tries to approximate as well as possible the completely random state within a limited supercell size. Instead of the usual SQS generation procedure which searches for a configuration that matches the correlation functions calculated for the completely random state, we match our supercell model with the average 2, 3, and 4-body correlation functions of the 1400 structures in each (x_Y, T_{sinter}) ensemble. We employed the *mcsqs* code [24], originally developed for SQS generation, to perform the matching using a Monte Carlo procedure. Since the resulting configuration depends somewhat on the initial state used in the Monte Carlo procedure, we performed 36 independent *mcsqs* runs for each (x_Y, T_{sinter}). This was repeated twice corresponding to the two independent RXMC runs in Ref. [21]. This means that 72 supercell models consisting of 9×9×9

unit cells were prepared for each (x_Y, T_{sinter}) pair to be used in diffusivity calculations.

In this work, we performed diffusivity calculations on Y configurations at T_{sinter} = 1866 K, which is a typical sintering temperature, and at T_{sinter} = 853 K, to examine how the sintering temperature may affect the Y configuration and thus the proton conductivity (we note that the phase separation into Y-rich and Y-poor phases around $x_Y \sim 0.1$ was reported below 1773 K [25]; this low temperature is chosen more for the sake of comparison rather than to reproduce to the experimental situation). For comparison, 72 supercells with random configurations of single Y ions and Y-Y pairs were also prepared by simple random sampling without SQS generation. The averaged proton diffusivity in the supercells with the random configuration of single Y ions at x_Y = 0.07 was also used for checking the validity of the SQS approach for the diffusivity estimation. See Fig. S1 in Supplementary Information for the comparison between the averaged proton diffusivity in the supercells with random Y configurations and that in the SQSs, which are in reasonable agreement with each other.

2.2 Proton diffusivity

The potential barriers ΔE^{mig} of proton rotation and hopping in Y-doped $BaZrO_3$ have been evaluated by the nudged elastic band method in previous theoretical studies [12,17,19]. The calculated ΔE^{mig} are widely scattered depending on the local Y configuration around the migrating proton, ranging from 0.1 eV to 1.1 eV for proton rotation and from 0.02 eV to 1.0 eV for proton hopping. In the present study, the proton jump frequencies Γ in the crystal at a given temperature were estimated using our

reported potential barriers [19] (Fig. S2, Tables S1 and S2) according to the following equation,

$$\Gamma = \Gamma_0 \exp\left(-\frac{\Delta E^{\mathrm{mig}}}{k_{\mathrm{B}}T}\right) \quad (1)$$

where Γ_0 is the vibrational prefactor, k_{B} is the Boltzmann constant, and T is the temperature. Γ_0 was set to 10 THz for all rotational and hopping paths, which is a typical value for ionic jumps in crystals [26-30].

The proton diffusivity was estimated under the independent-particle approximation by solving the following master equation corresponding to the balance of the existence probability of a single particle at each site [31,32].

$$\frac{\partial}{\partial t} p_i(\mathbf{r}, t) = \sum_{j \in A_i} [(\Gamma_{ji} p_j(\mathbf{r} + \mathbf{s}_{ij}, t) - \Gamma_{ij} p_i(\mathbf{r}, t)], \quad (2)$$

where i and j are the site indexes in the supercell (i, j = 1, 2, …, n_{site}), n_{site} is the number of sites in the supercell, $p_i(\mathbf{r}, t)$ is the existence probability of the single particle at site i as a function of position $\mathbf{r}$ and time t, A_i is the set of all adjacent sites to site i, and Γ_{ij} and $\mathbf{s}_{ij}$ are the jump frequency and jump vector from site i to j, respectively. The first and second terms in the brackets of equation (2) correspond to the inflow and outflow of the existence probability at site i, respectively. This equation can easily be solved by performing a Fourier transform $P_i(\mathbf{Q}, t) = \int_{-\infty}^{+\infty} p_i(\mathbf{r}, \mathrm{t}) \exp(i\mathbf{Q}\mathbf{r})\, \mathrm{d}\mathbf{r}$ with respect to position $\mathbf{r}$. Each element of the diffusion coefficient tensor $\mathbf{D}$ can finally be obtained as the eigenvalue of the $n_{\mathrm{site}} \times n_{\mathrm{site}}$ jump matrix $\mathbf{\Lambda}$ with elements Λ_{ij},

$$\Lambda_{ij} = \Gamma_{ji} \exp(-i\mathbf{Q}\mathbf{s}_{ij}) - \delta_{ij} \sum_{j \in A_i} \Gamma_{ij}, \quad (3)$$

where δ_{ij} is the Kronecker delta. An appropriate $\mathbf{Q}$ vector with a small magnitude should be chosen for

estimating each element D_{mn} ($m, n = x, y, z$). See ref. [33] for details. In the case of the proton diffusion in the $BaZrO_3$ supercell, only D_{xx}, D_{yy}, and D_{zz} are nonzero values, and the proton diffusion coefficient was estimated as the average of these three elements in the present study.

The H-H interaction was additionally treated as the modified site blocking effect, meaning that protons cannot occupy more than one proton site around an oxide ion at the same time (See ref. [22]). This assumption is based on the relatively strong repulsive interaction between two protons bonding to the same oxide ion [17,22]. Specifically, the jump frequency from site i to j was modified by the probability that another proton occupies site j or the other three sites around the same oxide ion as site j, denoted by p_j^{OH}. A proton at site i can jump into site j with the probability $(1 - p_j^{\mathrm{OH}})$, leading to the modified jump frequency $(1 - p_j^{\mathrm{OH}})\Gamma_{ij}$. The p_j^{OH} can be estimated easily assuming thermal equilibrium based on the Fermi-Dirac distribution function. The correlation effect between successive proton jumps was also taken into consideration for estimating the proton diffusivity. This effect is attributed to the deviation from the thermal-equilibrium site occupancies at the sites involved in the previous jumps. In the present study, the proton diffusivity was corrected by estimating the time loss in oscillatory jumps between adjacent sites as detailed in ref. [22] (the accuracy of the correction was verified by comparison with KMC simulations). Note that the estimated correlation factor is not the physical correlation factor defined for the collective diffusion, both of which are identical in the case of dilute protons. The difference between the two correlation factors was assumed to be negligible in the present study by reason of the low site occupancy of protons (0.025 at most), which can be

rigorously estimated by means of the KMC simulations. The number of protons was set to be equal to the number of Y dopants in all calculations presented below, and no oxygen vacancies were considered; this corresponds to the ideal situation of 100 % hydration in Y-doped $BaZrO_3$. Note that the 100 % hydration is not reported to be achieved in experiments even at low temperatures (90 % at most) [34], and that the dehydration reaction proceeds at high temperatures above 700 K to further decrease the proton concentration.

3. Results & Discussion

3.1 Proton Diffusivity

The proton diffusivities were evaluated in multiple supercells at several Y concentrations (x_Y = 0.07, 0.15, 0.22, 0.30), where Y dopants are distributed in four types of configurations, i.e., thermal equilibrium configurations at 1866 K and 853 K (Σ_{1866K} and Σ_{853K}), and random configurations of single Y ions and Y-Y pairs (Σ_{random} and Σ_{pair}). The solid lines with solid symbols in Fig. 1 show the calculated proton diffusion coefficients as a function of inverse temperature. For reference, the calculated proton diffusion coefficients in the perfect crystal without neither H-H nor Y-H interactions (the ideal noninteracting model) are also shown by the black broken lines. In this temperature range, the proton diffusivities in the supercells with Y configurations in thermal equilibrium at 1866 K and 853 K (Σ_{1866K} and Σ_{853K}) are higher than those in the case of the random configuration of Y dopants (Σ_{random}). This trend is understandable considering the repulsive interaction between Y dopants in

thermal equilibrium at the two temperatures [21]. The repulsive interaction enhances Y-dopant isolation in Σ_{1866K} and Σ_{853K}, leading to the opposite deviation from the proton diffusivity in Σ_{random} to that in Σ_{pair} with Y-dopant association. The isolation trend of Y dopants gradually decays with increasing Y concentration (x_Y), resulting in less dependence of the proton diffusivity on Y configurations at higher x_Y.

The above explanation provides a qualitative understanding of the dependence of the proton diffusivity on Y configurations, i.e., enhanced Y isolation leads to higher diffusivity in Σ_{1866K} and Σ_{853K} compared to Σ_{random}. In the following subsections, we discuss the microscopic origin of the enhanced proton diffusivity through a quantitative comparison of the differences in three factors governing the proton diffusivity, i.e. Y-H interaction (*proton trapping*), preferential conduction (*complete percolation*), and H-H interaction (*trap-site filling & carrier blocking*), between the four types of Y configurations. Since the H-H interaction has a minor effect on the proton diffusivity, the minor interaction is first discussed in Sec. 3.2, and is neglected for the subsequent detailed discussion on the other two factors, i.e., Y-H interaction and preferential conduction, in Secs. 3.3 and 3.4.

3.2 H-H interaction

First, we evaluate the effect of H-H interaction by comparing the proton diffusivities with and without the H-H interactions. According to the literature [22], the H-H interaction causes two competing effects, *carrier blocking* and *trap-site filling*. *Carrier blocking* has a negative impact on

diffusivity due to protons interfering with the movements of other protons. *Trap-site filling*, on the other hand, has a positive effect: trap sites with low potential energies are occupied by a portion of the protons, and this prevents other protons from being trapped in the same trap sites. The broken lines with open symbols in Fig. 1 show the calculated proton diffusion coefficients without H-H interaction under the independent-particle approximation. The H-H interaction enhances the proton diffusivity regardless of Y concentration, indicating that the positive effect of trap-site filling exceeds the negative one of carrier blocking. The characteristics (i.e., local Y configurations) of the trap sites themselves will be discussed in Sec. 3.3.

Figure 2 shows the ratios of the calculated diffusion coefficients with and without H-H interaction, $D_{\mathrm{w/H\text{-}H}}$ and $D_{\mathrm{w/oH\text{-}H}}$, at various Y concentrations (x_{Y} = 0.07, 0.15, 0.22, 0.30) and temperatures (T = 600, 700, 800, 900, 1000 K), which we call *enhancement factors* hereafter. The enhancement factor tends to be higher at lower temperatures; this is reasonable because protons are more likely to occupy trap sites at lower temperatures, resulting in a more pronounced trap-site filling effect. On the other hand, the enhancement factor shows little dependence on the Y concentration except for x_{Y} = 0.07. This trend suggests that the increase of the positive effect of trap-site filling is cancelled out by the negative effects due to the increase in the number of trap sites and the potential well deepening at the trap sites with increasing Y concentrations. At the lowest Y concentration (x_{Y} = 0.07), the enhancement factor is smaller than those at higher Y concentrations; this can be explained by few trap sites with deep potential wells surrounded by several Y dopants, resulting in weak trap-site filling effect at x_{Y} = 0.07.

Concerning the dependence on the types of Y configurations (Σ_{1866K}, Σ_{853K}, Σ_{random}, and Σ_{pair}), the difference is more pronounced at lower Y concentrations. At x_Y = 0.22 and 0.30, the enhancement factors do not show a clear dependence on Y configurations, while those in Σ_{1866K} and Σ_{853K} are significantly lower than those in Σ_{random} and Σ_{pair} at x_Y = 0.07 and 0.15. The origin of the difference in the enhancement factor is the isolation trend of Y dopants in Σ_{1866K} and Σ_{853K}; this leads to fewer proton sites with deep potential wells (again, these sites will be discussed in Sec. 3.3), resulting in a weaker trap-site filling effect.

The enhancement factor by the H-H interaction is, however, 1.4 at most, and this is a rather minor effect as highlighted in Fig. 1. That is, the differences between the fully interacting models with Y-H/H-H interaction and the ideal noninteracting model (solid lines vs. black broken lines in Fig. 1) are much larger than the change due to H-H interaction (colored solid vs. broken lines in Fig. 1). Enhancement factors can be significant only when the number of carriers exceeds the number of clearly defined trap sites with much lower energy than other sites [22]. The low enhancement factors indicate that this is not the case in Y-doped $BaZrO_3$. Moreover, the dependence on the types of Y configurations (Σ_{1866K}, Σ_{853K}, Σ_{random} and Σ_{pair}) is maintained at any Y concentration regardless of the H-H interaction. Therefore, in the following subsections, the effects of Y-H interaction and preferential conduction are discussed based on the proton diffusivities without the H-H interactions (broken lines in Fig. 1).

3.3 Y-H interaction

The proton site energies and the potential barriers of proton rotation and hopping are drastically changed by Y-H interaction, mainly depending on the local configurations of Y dopants. All proton sites in the supercells are therefore classified by the local Y configuration as in our previous study [19]. Specifically, all proton sites are classified into 84 types by the Y configuration on the eight Zr sites adjacent to a proton site, i.e., the first-, second-, and third-nearest-neighbor Zr sites (1NN, 2NN, and 3NN Zr sites), shown in Fig. 3(a).

Figure 4(a) shows the averaged site energies with the standard deviations at the 84 proton site types in all supercells, where the site energies also depend on the Y configuration beyond the adjacent Zr sites. The site energies are shown as relative values with reference to that at the proton site without any adjacent Y dopant, which can be regarded as the trap-free region. See Table S3 in Supplementary Information for the pseudocode to estimate the site energies. In this figure, the proton site types are numbered in ascending order of the total number of Y dopants on the adjacent Zr sites, where a proton site type with higher site energy is assigned a lower site ID when two or more site types have the same number of adjacent Y dopants. Although a clear correlation between the site energy and the total number of Y dopant within 3NN sites cannot be seen in Fig. 4(a), a strong negative correlation between the site energy and the number of adjacent Y dopants becomes evident when considering only the 1NN and 2NN sites. Specifically, the 84 proton sites are divided into five groups by the number of Y dopants only in the 1NN and 2NN Zr sites as shown in Figs. 3(b)-(f), i.e., groups 0, 1, 2, 3, and 4. The group

ID represents the number of adjacent Y dopants in the four Zr sites. Figure 4(b) shows the proton site energies at all 84 proton sites, in which the proton sites are renumbered in the order of the group ID. The proton sites in the same group are additionally renumbered in the descending order of the site energy. A clear correlation can be seen in this figure, i.e., lower site energies are associated with larger numbers of adjacent Y dopants. This indicates that the local Y configuration on the four adjacent Zr sites is the key factor in determining the proton site energy.

In our previous study [19], only the proton sites with the triangular Y configuration in group 3 were focused on as the most dominant trap sites, since they have the highest proton existence probability at $x_Y = 0.20$. However, the proton sites in group 4 surrounded by more Y dopants have lower site energies, i.e., higher trapping strength, although they are less abundant than group 3. Therefore, the proton sites in groups 3 and 4 should have been defined as the trap sites for protons. Figures 5 (a) and (b) show the trap-site fractions and the proton existence probabilities at the trap sites, i.e., proton trapping probability, at 600 K based on the two definitions of trap sites. In both trap-site definitions of "group 3 only" and "groups 3 & 4", the fraction of trap sites depends on the type of Y configurations, increasing in the order of Σ_{1866K}, Σ_{853K}, Σ_{random} and Σ_{pair}. The trap-site fraction is inversely correlated with the proton diffusivity, which is reasonable in terms of the negative effect of trap sites on the proton diffusivity. However, the proton trapping probability has no correlation with the proton diffusivity in the case of the trap-site definition of "group 3 only". Figure 6 shows the relationship between the proton diffusion coefficient at 600 K and the proton trapping probability with

various definitions of trap sites. The orange squares and the blue triangles correspond to the trap-site definitions of "group 3 only" and "groups 3 & 4", respectively. Ideally, the diffusion coefficient decreases with increasing the proton trapping probability, i.e., a negative correlation should be observed in these plots. However, the plots in the definition of "group 3 only" are far from the ideal correlation, particularly at higher Y concentrations. On the other hand, the plots in the definition of "groups 3 and 4" approach the ideal negative correlation, meaning that the proton sites in both groups 3 and 4 are identified as the main trap sites for protons in Y-doped $BaZrO_3$.

Note that the difference between Σ_{1866K} and Σ_{853K} still deviates from the ideal negative correlation, suggesting that the definition of trap sites remains insufficient. Focusing on the site energies in group 2, several proton sites have low site energies comparable to those in group 3. Such low-energy proton sites have a common Y configuration, i.e., a Y-Y pair occupying the adjacent 1NN and 2NN Zr sites as shown in Fig. 3(g). These low-energy proton sites in group 2 are called group 2' hereafter. Figure 5(c) shows the trap-site fractions and the proton trapping probabilities at 600 K when all proton sites in groups 2', 3, and 4 are defined as the trap sites. The green diamonds in Fig. 6 correspond to the third definition of trap sites (groups 2', 3, and 4), which are now consistent with the ideal negative correlation between the proton diffusivity and the proton existence probability at the defined trap sites. Therefore, the proton sites in group 2' should also be considered as trap sites. Note that proton sites surrounded by a Y dopant are not regarded as effective trap sites, even though the Y dopant is located at the 1NN or 2NN Zr sites. This is of importance in understanding the effect of proton trapping in this

system.

We can now reconcile the impact of Y configuration on the proton diffusivity based on the above definition of trap sites. That is, the Y configuration in the thermal equilibrium state at higher temperatures tends to form less trap sites, resulting in higher proton diffusivity. This is attributed to the repulsive interaction between Y dopants, suggesting that the isolation of Y dopants in the crystal is a reasonable strategy for improving the proton conductivity.

3.4 Preferential conduction

The preferential conduction along the YO_6 network is also a key factor in determining the proton diffusivity. The *optimal path* is here defined as the long-range migration path between two most stable sites separated by a lattice translation vector of the 9×9×9 supercell with the lowest potential barrier, i.e., the difference between the highest transition state energy and the lowest site energy along the long-range migration path. The optimal path was explored by the dynamic-programming-based algorithm in the present study (See ref. [35] for details). The site energy at the highest-energy proton site along the optimal path vs. that in the entire supercell ($E_{\mathrm{opt}}^{\mathrm{high}}$) is a direct indicator for the preferential conduction.

Taking the random configuration of Y dopants (Σ_{random}) as an example, the normalized site-energy distribution in the 72 supercells at each Y concentration is shown in Fig. 7 (See Fig. S3 in Supplementary Information for $\Sigma_{1866\mathrm{K}}$, $\Sigma_{853\mathrm{K}}$, and Σ_{pair}). The site energy is expressed as the relative

energy with reference to the highest energy site in each supercell. The proton existence probability at 600 K is also shown in each figure. In addition, the normalized histograms of the lowest and highest site energies along the optimal paths in the 72 supercells are shown by the blue and red bars, respectively. Regardless of Y concentration, the normalized site-energy distribution exhibits a single peak close to 0 eV and a single or double peak around –0.15 eV, which are attributed to the proton sites in group 0 and group 1, respectively. Although the site-energy distributions of the other groups seem negligibly small, these sites also play a key role in the proton diffusivity. In fact, the proton existence probabilities are higher at these sites with lower site energies than those in groups 0 and 1. The lowest site energy ($E_{\mathrm{opt}}^{\mathrm{low}}$) exhibits a declining trend with the Y concentration.

Focusing on the highest energy sites along the optimal paths, they all belong to group 0 at $x_{\mathrm{Y}} = 0.07$, meaning that protons migrate over a long range via trap-free regions. This conduction mechanism is close to the conventional picture of carrier conduction in a crystal with dilute dopants, i.e., *trapping and detrapping* employed by Yamazaki et al. in Ref. [18]. On the other hand, the highest energy sites belong to group 1 in most cases at $x_{\mathrm{Y}} \geq 0.15$. This indicates that the preferential proton conduction occurs along the YO_6 network and that protons are not required to visit trap-free regions for their long-range migration.

Figure 8 shows the averaged $E_{\mathrm{opt}}^{\mathrm{low}}$ and $E_{\mathrm{opt}}^{\mathrm{high}}$ in all 72 supercells in each Y configuration ($\Sigma_{1866\mathrm{K}}$, $\Sigma_{853\mathrm{K}}$, Σ_{random}, and Σ_{pair}) as a function of Y concentration. At $x_{\mathrm{Y}} = 0.07$, $E_{\mathrm{opt}}^{\mathrm{high}}$ are close to 0 eV in all Y configurations, indicating no preferential conduction at the low Y concentration. On the other hand,

E_{opt}^{low} depends on the Y configurations, which decreases in the order of Σ_{1866K}, Σ_{853K}, Σ_{random}, and Σ_{pair}. Therefore, the difference in the energy distribution of the trap sites is the main factor for the difference in the proton diffusivity between the Y configurations at the low Y concentration. At x_Y = 0.15, the preferential conduction of protons starts appearing in most of the supercells with a few exceptions (See Fig. S3). The fraction of the exceptions increases in the order of Σ_{1866K}, Σ_{853K}, Σ_{random} and Σ_{pair}, corresponding to the increasing tendency of the averaged E_{opt}^{high}. This indicates that the preferential conduction pathways are more readily formed with higher isolation trend of Y dopants at the relatively low Y concentration. In contrast, E_{opt}^{high} decreases in the same order at the highest Y concentration (x_Y = 0.30), where the association of Y dopants makes the YO_6 network more developed. Thus, the effects of isolation and association trends of Y dopants change depending on the Y concentration. Concerning E_{opt}^{low}, the difference between the four types of Y configurations becomes smaller with increasing Y concentration. Hence, the proton diffusivities in the four types of Y configurations are close to each other at the highest Y concentration (Fig. 1(d)).

Note that the preferential conduction on the proton diffusivity has a minor effect compared to the proton trapping effect. E_{opt}^{low} and E_{opt}^{high} are indicators for the proton trapping and the preferential conduction, respectively, meaning that the changes in the two indicators depending on the Y concentration are important for discussion of the dominant factor determining the proton diffusivity. Taking the Σ_{1866K} configuration of Y dopants as the most realistic condition, E_{opt}^{low} and E_{opt}^{high} decrease with increasing the Y concentration x_Y in the range from 0.07 to 0.30 by –0.29 eV and –0.15 eV,

respectively. The smaller change in E_{opt}^{high} indicates the minor impact of the preferential conduction on the proton diffusivity, resulting in a declining trend of the proton diffusivity (See Fig. S4 in Supplementary Information) due to the major impact of the proton trapping. The declining trend in this work is in reasonable agreement with the experimentally-reported proton conductivity and diffusivity [34], but is opposite to the rising trend of the proton mobility reported in Ref. [17]. This discrepancy is probably due to the underestimation of the proton trapping effect in Ref. [17], which originates from the simple assumption of two-valued site energies. Another possible source of this discrepancy is in the treatment of finite-size supercell effects in calculating the potential barriers for proton jumps; we employed a relatively large (4×4×4 cubic perovskite) supercell and made no *a posteriori* corrections, while Ref. [17] performed finite-size corrections of some sort although no details were given. Such differences apparently led to drastically different potential barriers for certain Y configurations (e.g., we report a potential barrier of 0.05 eV for proton hopping H3-2 in Table S1 while Ref. [17] reports 0.66 eV).

Conclusions

In the present study, we theoretically revisited the proton diffusivity in Y-doped $BaZrO_3$ with realistic dopant configurations under processing conditions. The findings of the present study are summarized below:

1. The estimated proton diffusivity with the realistic Y configurations are basically higher than that

with the random configuration. This is due to the isolation trend of Y dopants at thermal equilibrium, which decreases the number of trap sites with deep potential wells.

2. The proton trapping by Y-H interaction is the most dominant factor governing the proton diffusivity in the crystal compared to the other two factors, i.e., preferential conduction along the 3D network of Y dopants and H-H interaction.

3. The above to findings suggest that a reasonable strategy for improving the proton diffusivity is suppressing the negative impact of *proton trapping* by controlling the dopant configuration in the crystal, rather than enhancing the positive impact of *preferential conduction*. Specifically, Y dopants should be isolated as much as possible from each other, which is different from the previously proposed strategy in Ref. [17] that the preferential conduction network is developed as much as possible by forming superstructure of Y dopants in the crystal.

Acknowledgment

This work was partially supported by JSPS KAKENHI granted to K.T. (20H02422) and to S.K. (19K15287). The RXMC calculations were performed using ab Initio Configurational Sampling toolkit (abICS) [https://www.pasums.issp.u-tokyo.ac.jp/abics/en/] on joint-use supercomputing facilities at the Institute for Solid State Physics, the University of Tokyo. S.K. is also supported by CREST, Japan Science and Technology Agency (JPMJCR18J3).

References

1 K. D. Kreuer, *Solid State Ionics*, 1999, **125**, 285.

2 K. Katahira, Y. Kohchi, T. Shimura and H. Iwahara, *Solid State Ionics*, 2000, **138**, 91.

3 Y. Yamazaki, R. Hernandez-Sanchez and S. M. Haile, *Chem. Mater.*, 2009, **21**, 2755.

4 D. Pergolesi, E. Fabbri, A. D. Epifanio, E.D. Bartolomeo, A. Tebano, S. Sanna, S. Licoccia, G. Balestrino and E. Traversa, *Nat. Mater.*, 2010, **9**, 846.

5 D. Han, Y. Nose, K. Shinoda and T. Uda, *Solid State Ionics*, 2012, **213**, 2.

6 F. Giannici, M. Shirpour, A. Longo, A. Martorana, R. Merkle and J. Maier, *Chem. Mater.*, 2011, **23**, 2994–3002.

7 D. Han, K. Kishida, K. Shinoda, H. Inui and T. Uda, *J. Mater. Chem. A*, 2013, **1**, 3027–3033.

8 D. Han and T. Uda, *J. Mater. Chem. A*, 2018, **6**, 18571-18582.

9 T. Omata, Y. Noguchi and S. Otsuka-Yao-Matsuo, *J. Electrochem. Soc.*, 2005, **152**, E200-E205.

10 I. Oikawa and H. Takamura, *Chem. Mater.*, 2015, **27**, 6660-6667.

11 W. Münch, K. D. Kreuer, G. Seifert and J. Maier, *Solid State Ionics*, 2000, **136-137**, 183.

12 S. G. Kang and D. S. Sholl, *RSC Adv.*, 2013, **3**, 3333-3341.

13 M. A. Gomez, M. A. Griffin, S. Jindal, K. D. Rule and V. R. Cooper, *J. Chem. Phys.*, 2005, **123**, 094703.

14 M. E. Björketun, P. G. Sundell, G.Wahnström and D. Engberg, *Solid State Ionics*, 2005, **176**, 3035.

15 N. Bork, N. Bonanos, J. Rossmeisl and T. Vegge, *Phys. Rev. B*, 2010, **82**, 014103.

16 K. Toyoura, D. Hirano, A. Seko, M. Shiga, A. Kuwabara, M. Karasuyama, K. Shitara and I. Takeuchi, *Phys. Rev. B*, 2016, **93**, 054112.

17 F. M. Draber, C. Ader, J. P. Arnold, S. Eisele, S. Grieshammer, S. Yamaguchi and M. Martin, *Nat. Mater.*, 2019, **19**, 338–346.

18 Y. Yamazaki, F. Blanc, Y. Okuyama, L. Buannic, J. C. Lucio-Vega, C. P. Grey and S. M. Haile, *Nat. Mater.*, 2013, **12**, 647.

19 K. Toyoura, W. Meng, D. Han and T. Uda, *J. Mater. Chem. A*, 2018, **6**, 22721.

20 H. Takahashi, I. Yashima, K. Amezawa, K. Eguchi, H. Matsumoto, H. Takamura and S. Yamaguchi, *Chem. Mater.*, 2017, **29**, 1518.

21 S. Kasamatsu, O. Sugino, T. Ogawa and A. Kuwabara, *J. Mater. Chem. A*, 2020, **8**, 12674-12686.

22 K. Toyoura, T. Fujii, N. Hatada, D. Han and T. Uda, *J. Phys. Chem. C.*, 2019, **123**, 26823.

23 A. Zunger, S. H. Wei, L. G. Ferreira and J. E. Bernard, *Phys. Rev. Lett.*, 1990, **65**, 353–356.

24 A. van de Walle, P. Tiwary, M. M. de Jong, D. L. Olmsted, M. D. Asta, A. Dick, D. Shin, Y. Wang, L. Q. Chen and Z. K. Liu, *Calphad*, 2013, **42**, 13.

25 K. Ueno, N. Hatada, D. Han, K. Toyoura and T. Uda, *J. Solid State Electrochem.*, 2020, **24**, 1523-1538.

26 R. Yu and L. C. De Jonghe, *J. Phys. Chem. C*, 2007, **111**, 11003.

27 K. Toyoura, Y. Koyama, A. Kuwabara, F. Oba and I. Tanaka, *Phys. Rev. B*, 2008, **78**, 214303.

28 K. Toyoura, N. Hatada, Y. Nose, I. Tanaka, K. Matsunaga and T. Uda, *J. Phys. Chem. C*, 2012, **116**, 19117.

29 N. Hatada, K. Toyoura, T. Onishi, Y. Adachi and T. Uda, *J. Phys. Chem. C*, 2014, **118**, 29629.

30 K. Toyoura, A. Nakamura and K. Matsunaga, *J. Phys. Chem. C*, 2015, **119**, 8480.

31 C. T. Chudley and R. J. Elliott, *Proc. Phys. Soc.*, 1961, **77**, 353.

32 R. Hempelmann, *Quasielastic Neutron Scattering and Solid State Diffusion*, Oxford University Press Inc., New York, 2000.

33 K. Toyoura, T. Fujii, K. Kanamori and I. Takeuchi, *Phys. Rev. B*, 2020, **101**, 184117.

34 D. Han, N. Hatada and T. Uda, *J. Am. Ceram. Soc.*, 2016, **99**, 3745–3753.

35 K. Kanamori, K. Toyoura, J. Honda, K. Hattori, A. Seko, M. Karasuyama, K. Shitara, M. Shiga, A. Kuwabara and I. Takeuchi, *Phys. Rev. B*, 2018, **97**, 125124.

Figure captions

Figure 1. The calculated proton diffusion coefficients as a function of inverse temperature in various Y configurations. The Y concentration, i.e., the site occupancy on the Zr sites x_Y, is (a) 0.07, (b) 0.15, (c) 0.22, and (d) 0.3. The solid and broken lines denote the proton diffusion coefficients with and without the H-H interaction. The black broken lines show the proton diffusion coefficients in the perfect crystal with neither H-H nor Y-H interaction.

Figure 2. The temperature and Y-configuration dependences of the enhancement factors by the H-H interaction. The Y concentration, i.e., the site occupancy on the Zr sites x_Y, is (a) 0.07, (b) 0.15, (c) 0.22, and (d) 0.3.

Figure 3. (a) The 1NN, 2NN, and 3NN Zr sites adjacent to a proton site. The proton sites are classified into 84 types according to the local Y configurations on the eight Zr sites. (b)–(g) Local Y configurations on the 1NN and 2NN Zr sites corresponding to the proton sites in groups 0, 1, 2, 3, 4 and 2', respectively. Note that only an example of multiple local Y configurations is illustrated for groups 1, 2, and 3.

Figure 4. The averaged site energies with the standard deviations at 84 proton site types in all supercells. The site energies are shown as the relative values with reference to that at the proton site without any adjacent Y dopant. The proton site types are numbered in the ascending order of the total number of Y dopants (a) on the 1NN, 2NN, and 3NN Zr sites and (b) on the 1NN and 2NN Zr sites. The proton site types with the same number of adjacent Y dopants are additionally renumbered in the descending order of the site energy.

Figure 5. The site fractions and proton existence probabilities at 600 K (H^+ prob.) of the proton sites (a) in group 3 only, (b) in groups 3 and 4, and (c) in groups 2', 3, and 4, which depend on the types of Y configurations (Σ_{1866K}, Σ_{853K}, Σ_{random} and Σ_{pair}).

Figure 6. The relationship between the proton diffusion coefficient at 600 K and the proton existence probability (H^+ prob.) at trap sites when varying Y concentrations, i.e., x_Y = (a) 0.07, (b) 0.15, (c) 0.22,

and (d) 0.30. The trap sites are here defined in three ways, i.e., “group 3 only”, “groups 3 & 4”, and “groups 2’, 3 & 4”.

Figure 7. The normalized site-energy distributions (Dist.) in the 72 supercells at various Y concentrations, in the case of the random configuration of Y dopants (Σ_{random}). The proton existence probability at 600 K (H^+ prob.) is also shown in each figure. The normalized histograms of the lowest and highest site energy levels along the optimal paths (E_{opt}^{low} and E_{opt}^{high}) in the 72 supercells are shown on the right sides of each figure by the blue and red bars, respectively.

Figure 8. The averaged lowest and highest site energies along the optimal paths, E_{opt}^{low} and E_{opt}^{high}, in all 72 supercells in each type of Y configuration (Σ_{1866K}, Σ_{853K}, Σ_{random}, and Σ_{pair}) as a function of Y concentration.

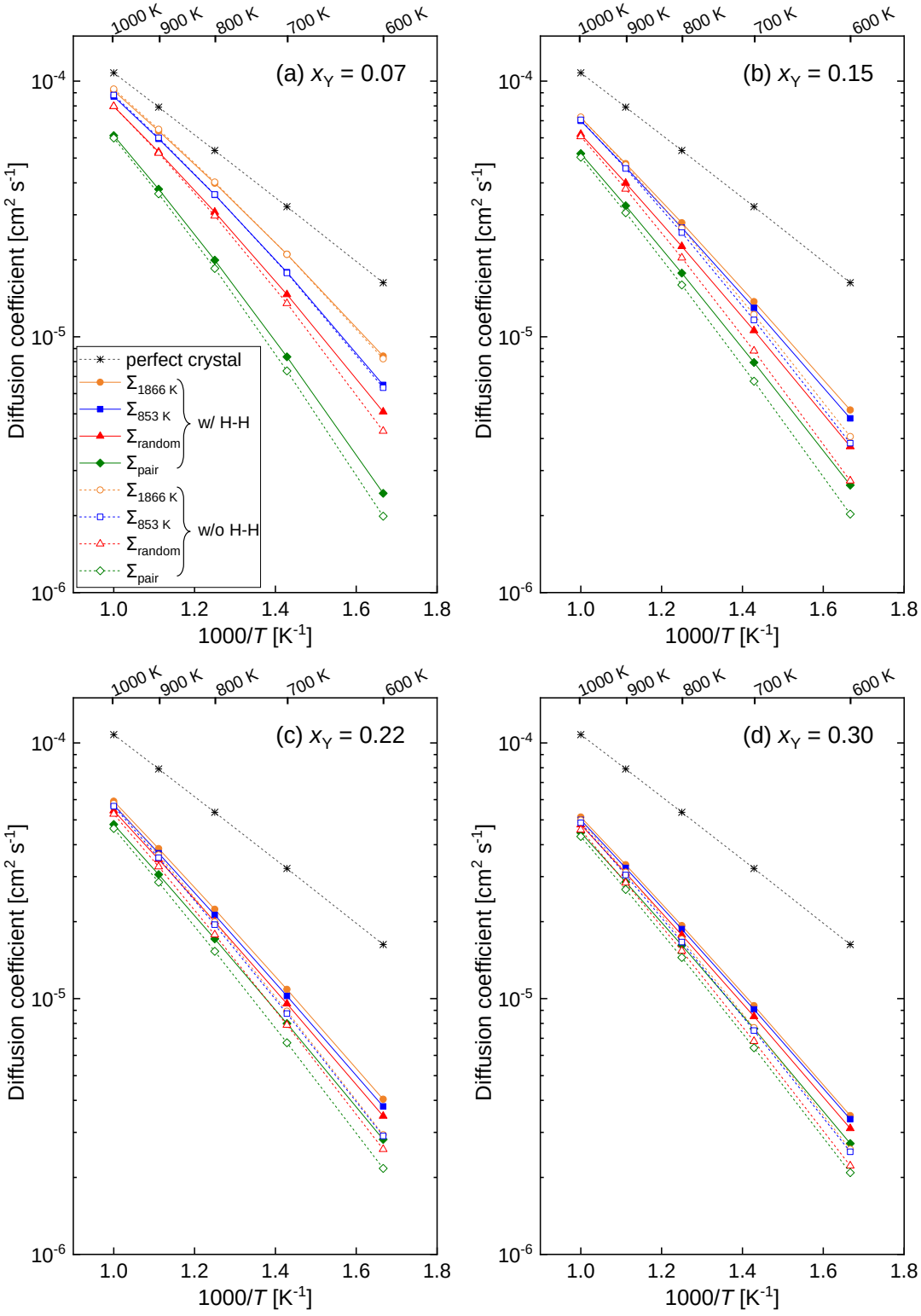

Figure 1. The calculated proton diffusion coefficients as a function of inverse temperature in various Y configurations. The Y concentration, i.e., the site occupancy on the Zr sites x_Y, is (a) 0.07, (b) 0.15, (c) 0.22, and (d) 0.3. The solid and broken lines denote the proton diffusion coefficients with and without the H-H interaction. The black broken lines show the proton diffusion coefficients in the perfect crystal with neither H-H nor Y-H interaction.

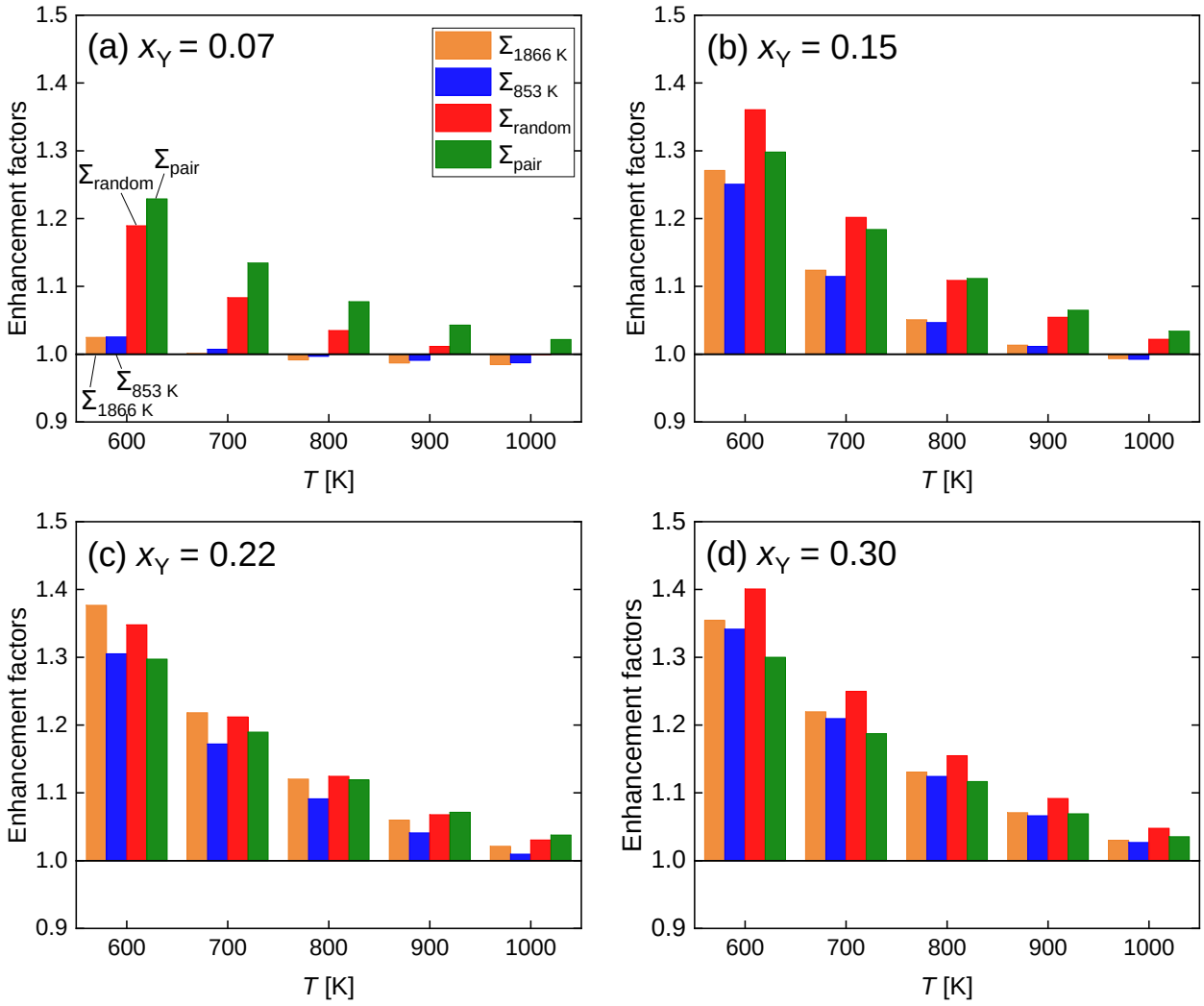

Figure 2. The temperature and Y-configuration dependences of the enhancement factors by the H-H interaction. The Y concentration, i.e., the site occupancy on the Zr sites x_Y, is (a) 0.07, (b) 0.15, (c) 0.22, and (d) 0.3.

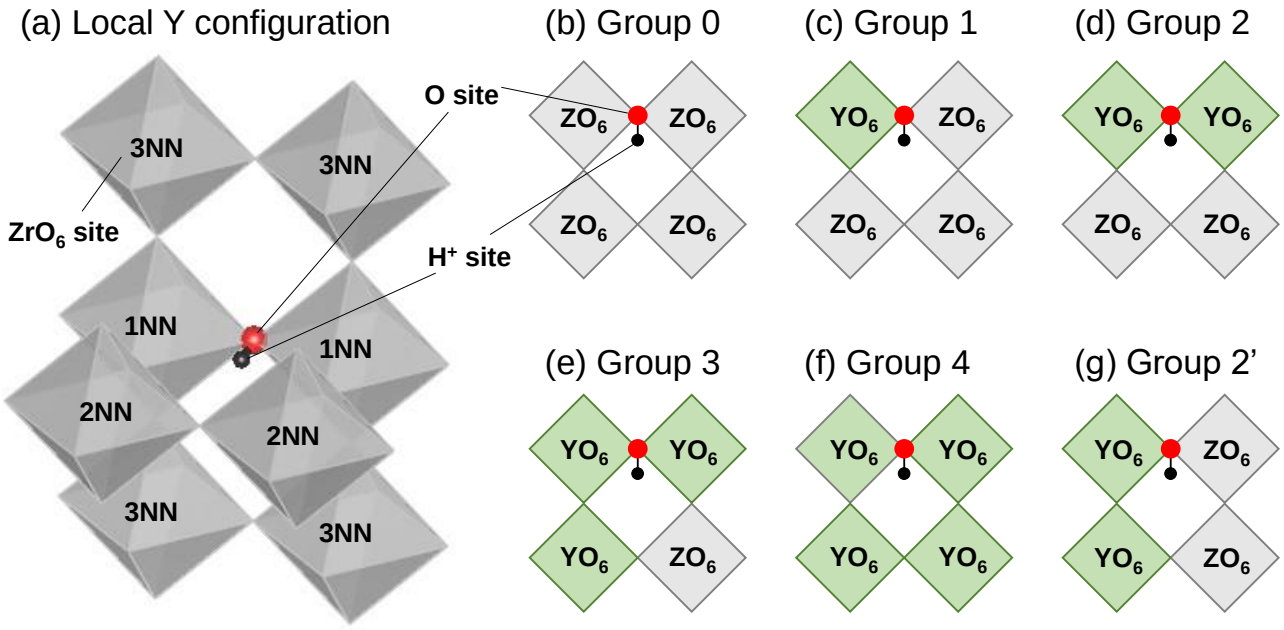

Figure 3. (a) The 1NN, 2NN, and 3NN Zr sites adjacent to a proton site. The proton sites are classified into 84 types according to the local Y configurations on the eight Zr sites. (b)–(g) Local Y configurations on the 1NN and 2NN Zr sites corresponding to the proton sites in groups 0, 1, 2, 3, 4 and 2', respectively. Note that only an example of multiple local Y configurations is illustrated for groups 1, 2, and 3.

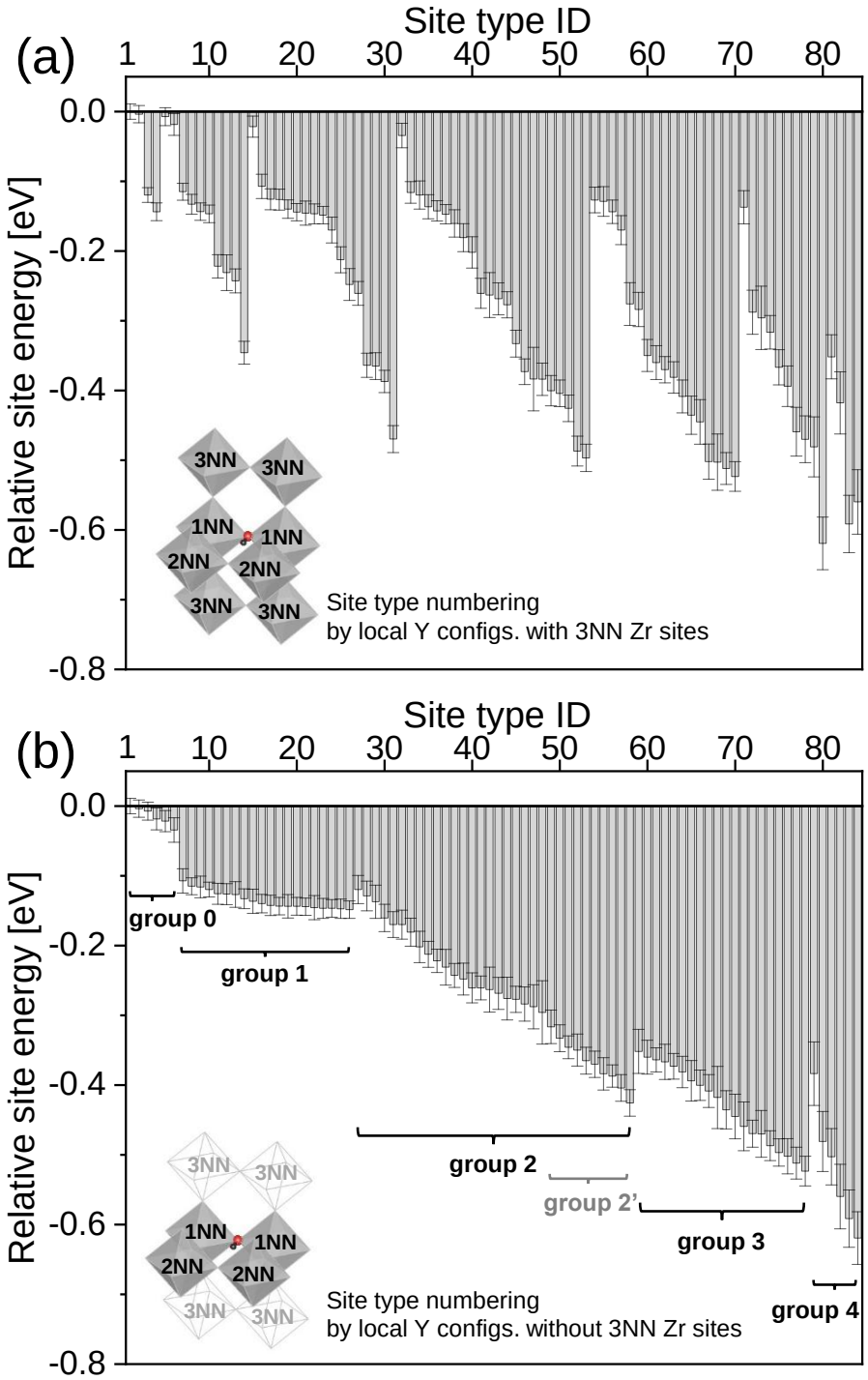

Figure 4. The averaged site energies with the standard deviations at 84 proton site types in all supercells. The site energies are shown as the relative values with reference to that at the proton site without any adjacent Y dopant. The proton site types are numbered in the ascending order of the total number of Y dopants (a) on the 1NN, 2NN, and 3NN Zr sites and (b) on the 1NN and 2NN Zr sites. The proton site types with the same number of adjacent Y dopants are additionally renumbered in the descending order of the site energy.

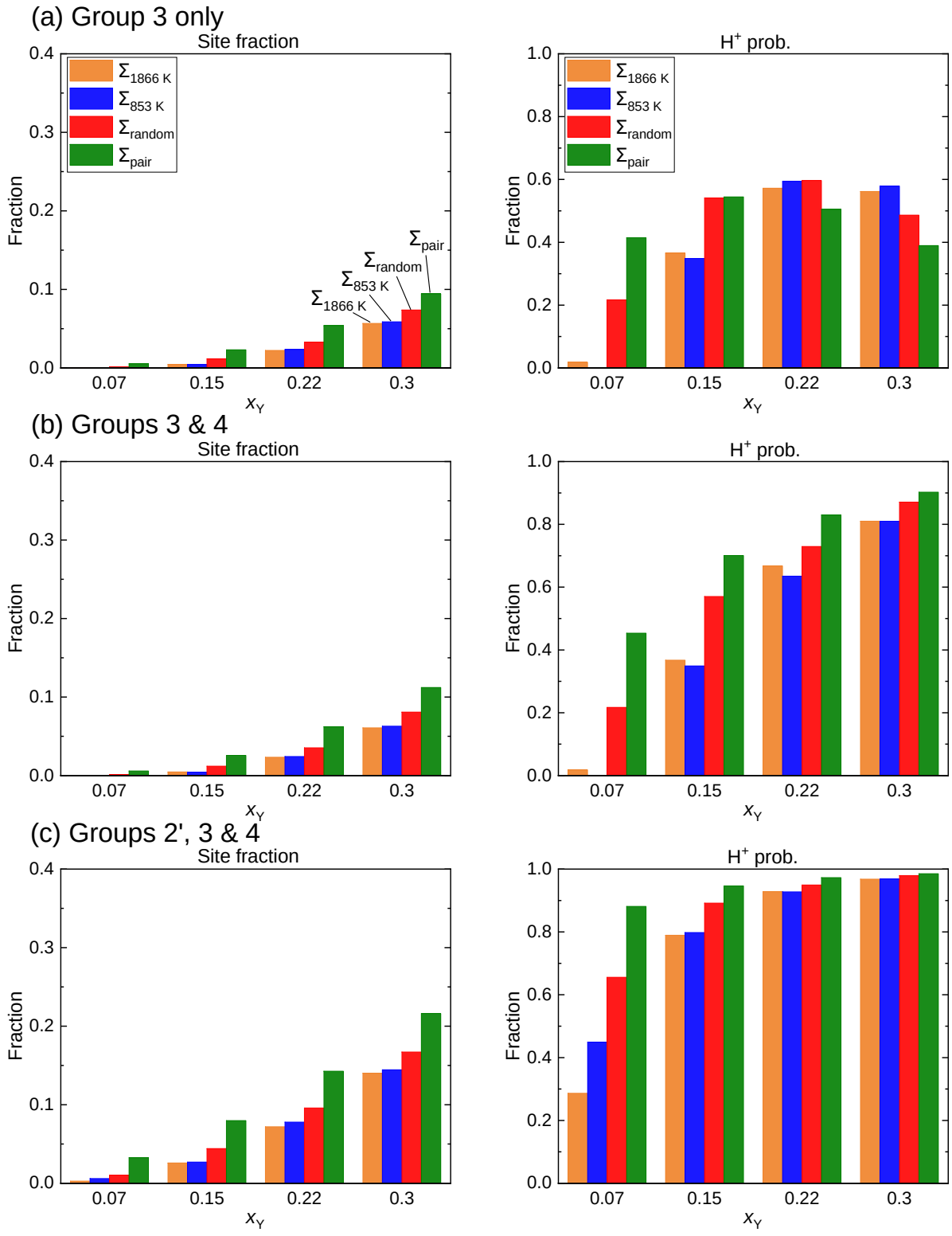

Figure 5. The site fractions and proton existence probabilities at 600 K (H^+ prob.) of the proton sites (a) in group 3 only, (b) in groups 3 and 4, and (c) in groups 2', 3, and 4, which depend on the types of Y configurations (Σ_{1866K}, Σ_{853K}, Σ_{random} and Σ_{pair}).

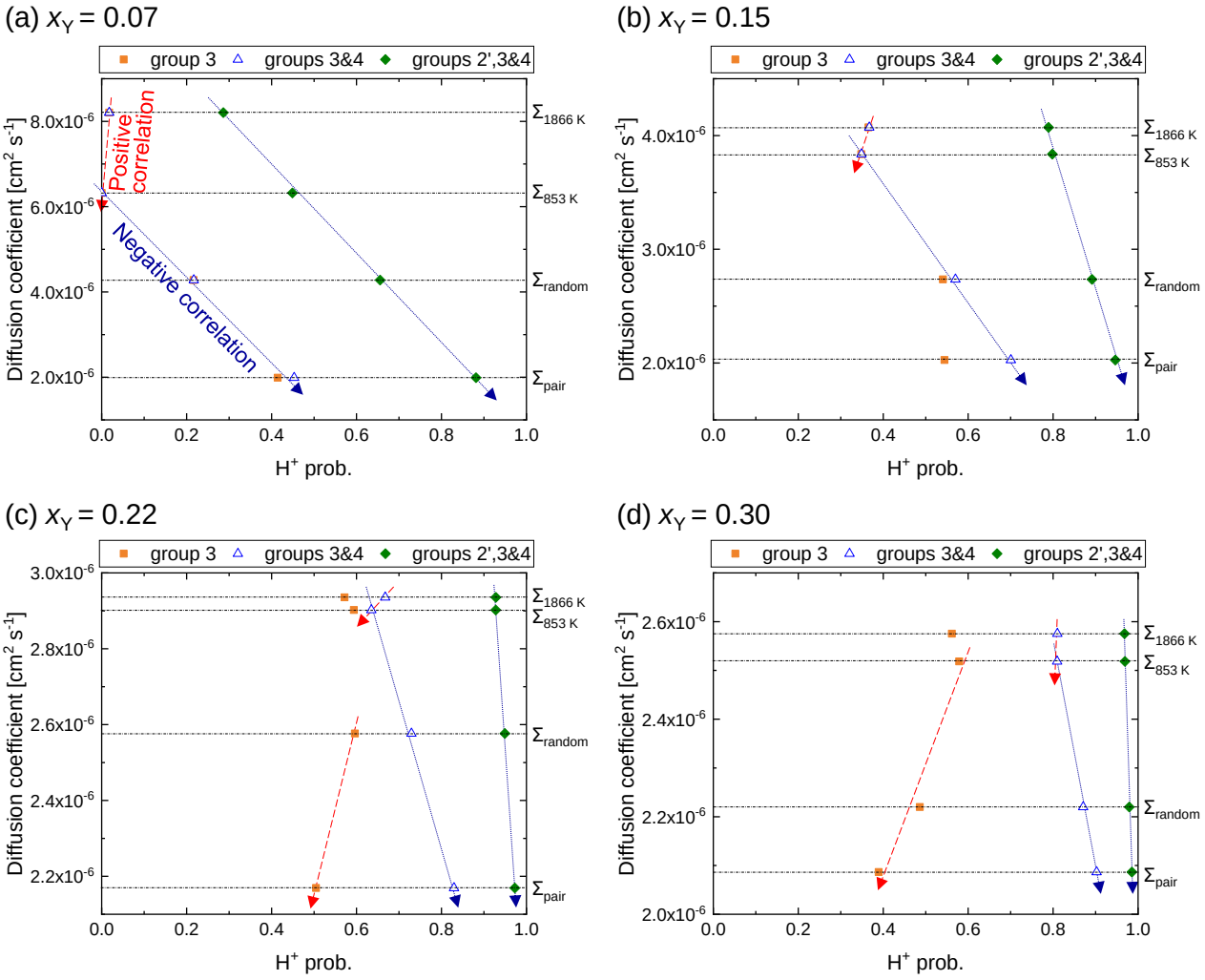

Figure 6. The relationship between the proton diffusion coefficient at 600 K and the proton existence probability (H^+ prob.) at trap sites when varying Y concentrations, i.e., x_Y = (a) 0.07, (b) 0.15, (c) 0.22, and (d) 0.30. The trap sites are here defined in three ways, i.e., “group 3 only”, “groups 3 & 4”, and “groups 2’, 3 & 4”.

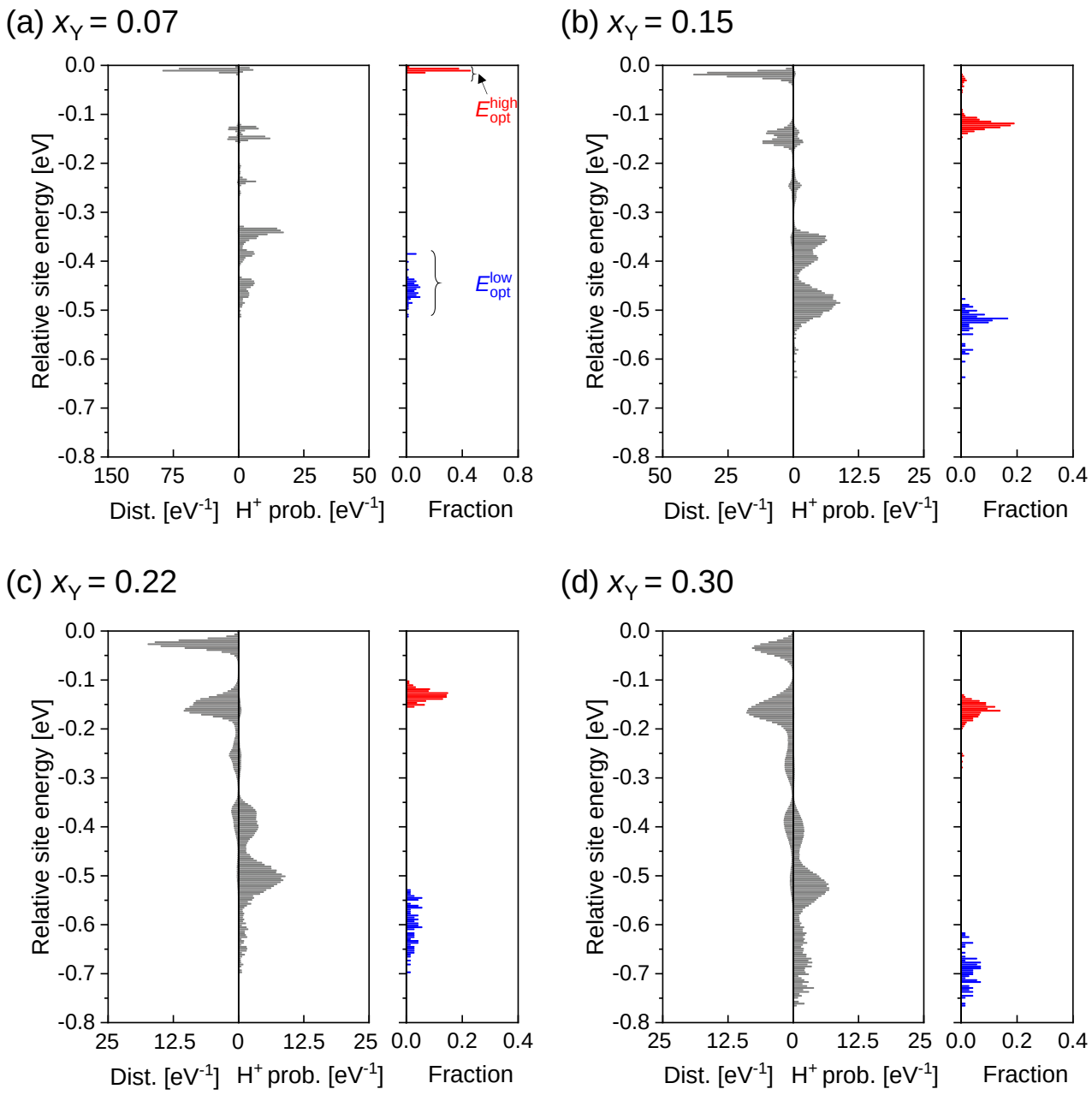

Figure 7. The normalized site-energy distributions (Dist.) in the 72 supercells at various Y concentrations, in the case of the random configuration of Y dopants (Σ_{random}). The proton existence probability at 600 K (H^+ prob.) is also shown in each figure. The normalized histograms of the lowest and highest site energy levels along the optimal paths (E_{opt}^{low} and E_{opt}^{high}) in the 72 supercells are shown on the right sides of each figure by the blue and red bars, respectively.

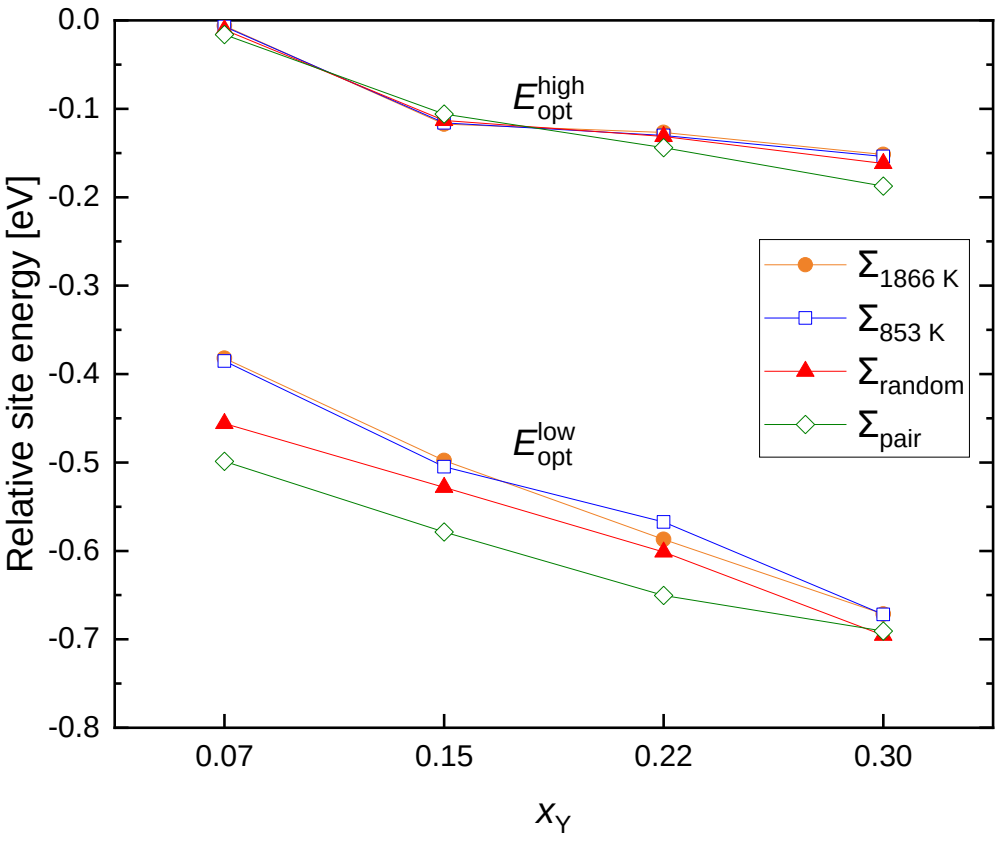

Figure 8. The averaged lowest and highest site energies along the optimal paths, E_{opt}^{low} and E_{opt}^{high}, in all 72 supercells in each type of Y configuration (Σ_{1866K}, Σ_{853K}, Σ_{random}, and Σ_{pair}) as a function of Y concentration.

Supplementary Information

Theoretical study on proton diffusivity in Y-doped $BaZrO_3$ with realistic dopant configurations

Takeo Fujii[1], Kazuaki Toyoura[*,1], Tetsuya Uda[1], and Shusuke Kasamatsu[**,2]

[1] *Department of Materials Science and Engineering, Kyoto University, Kyoto 606-8501, Japan*

[2] *Academic Assembly (Faculty of Science), Yamagata University, Yamagata 990-8560, Japan*

* toyoura.kazuaki.5r@kyoto-u.ac.jp

** kasamatsu@sci.kj.yamagata-u.ac.jp

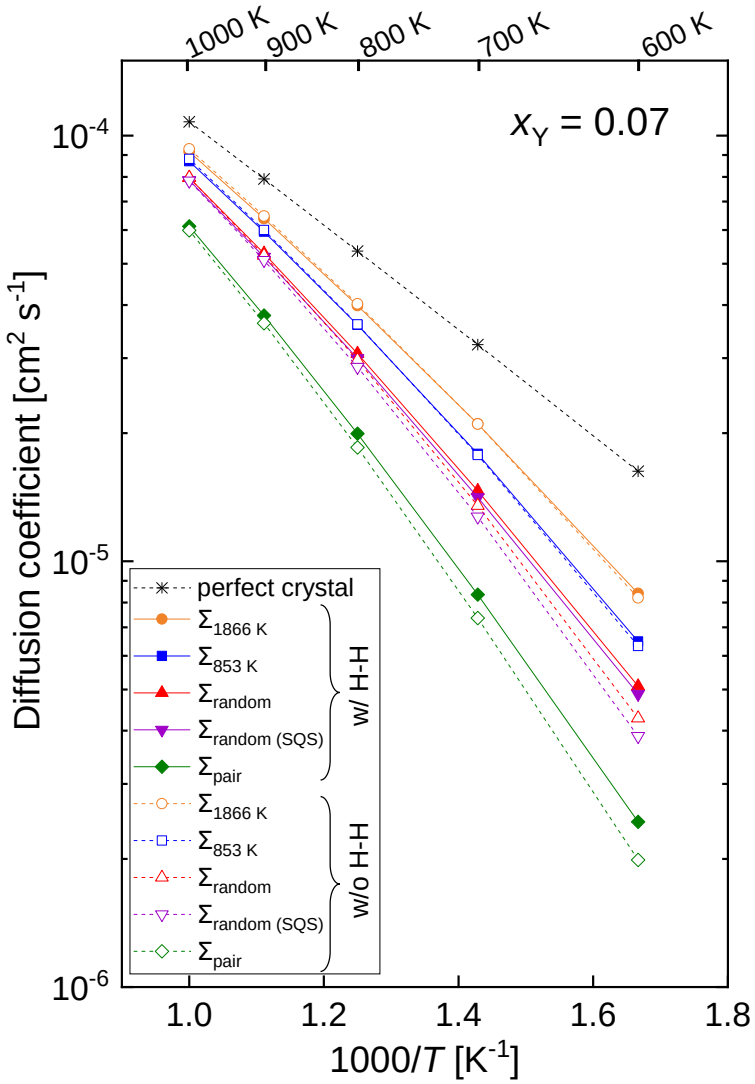

Figure S1. The calculated proton diffusion coefficients as a function of inverse temperature in various Y configurations at $x_Y = 0.07$. The solid and broken lines denote the proton diffusion coefficients with and without the H-H interaction. The purple lines show the proton diffusion coefficients in the SQSs corresponding to the random Y configuration (Σ_{random}). The black broken lines is the proton diffusion coefficients in the perfect crystal with neither H-H nor Y-H interaction.

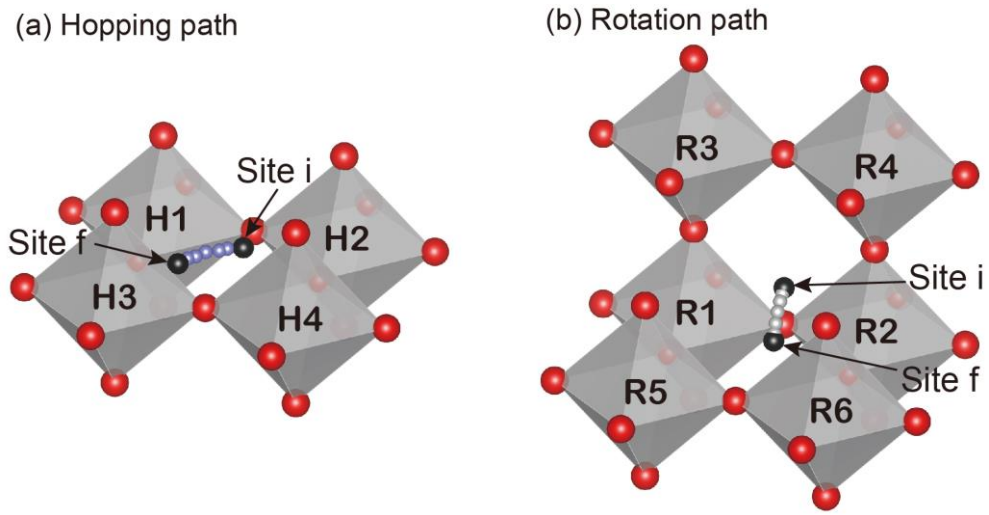

Figure S2. Adjacent Zr sites around the proton (a) hopping and (b) rotation paths, which were taken into consideration for Y local configuration [19]. Protons on sites i and f in the rotation path form an OH bond with the same O ion between R1 and R2. The site i is located on the plane through "R1, R2, R3, and R4", while the site f is on the plane through "R1, R2, R5, and R6". In the hopping path, sites i and f are located on the same plane as H1, H2, H3, and H4, forming an OH bond with the different O ions between "H1 and H2" and "H1 and H3", respectively.

Table S1. Calculated potential barriers of proton hopping with various configurations of Y dopants in Zr sites [19].

		Zr and Y configuration in B sites				$\Delta E_{i\to f}^{mig}$ / eV	$\Delta E_{f\to i}^{mig}$ / eV
# of Y	Path ID	H1	H2	H3	H4		
0	H0-1	Zr	Zr	Zr	Zr	0.25	0.25
1	H1-1	Y	Zr	Zr	Zr	0.21	0.21
	H1-2	Zr	Zr	Y	Zr	0.19	0.17
	H1-3	Zr	Zr	Zr	Y	0.42	0.42
2	H2-1	Y	Zr	Y	Zr	0.15	0.02
	H2-2	Y	Zr	Zr	Y	0.41	0.41
	H2-3	Zr	Zr	Y	Y	0.24	0.34
	H2-4	Zr	Y	Y	Zr	0.13	0.13
3	H3-1	Y	Zr	Y	Y	0.24	0.38
	H3-2	Y	Y	Y	Zr	0.05	0.05
	H3-3	Zr	Y	Y	Y	0.56	0.56
4	H4-1	Y	Y	Y	Y	0.45	0.45

Table S2. The calculated potential barriers of proton rotation with various configurations of Y dopants in Zr sites [19].

		Zr and Y configuration in B sites						$\Delta E_{\mathrm{i\to f}}^{\mathrm{mig}}$ / eV	$\Delta E_{\mathrm{f\to i}}^{\mathrm{mig}}$ / eV
# of Y	Path ID	R1	R2	R3	R4	R5	R6		
0	R0-1	Zr	Zr	Zr	Zr	Zr	Zr	0.17	0.17
1	R1-1	Y	Zr	Zr	Zr	Zr	Zr	0.18	0.18
	R1-2	Zr	Zr	Zr	Zr	Y	Zr	0.11	0.25
2	R2-1	Y	Y	Zr	Zr	Zr	Zr	0.25	0.25
	R2-2	Zr	Zr	Zr	Zr	Y	Y	0.09	0.31
	R2-3	Zr	Zr	Y	Zr	Y	Zr	0.20	0.20
	R2-4	Zr	Zr	Zr	Y	Y	Zr	0.17	0.17
	R2-5	Y	Zr	Zr	Zr	Y	Zr	0.08	0.29
	R2-6	Y	Zr	Zr	Zr	Zr	Y	0.11	0.22
3	R3-1	Zr	Zr	Y	Zr	Y	Y	0.20	0.32
	R3-2	Y	Zr	Y	Zr	Y	Zr	0.20	0.20
	R3-3	Y	Zr	Zr	Y	Zr	Y	0.20	0.20
	R3-4	Y	Zr	Zr	Zr	Y	Y	0.24	0.49
	R3-5	Y	Zr	Zr	Y	Y	Zr	0.08	0.37
	R3-6	Y	Y	Zr	Zr	Y	Zr	0.13	0.33
4	R4-1	Zr	Zr	Y	Y	Y	Y	0.17	0.17
	R4-2	Y	Y	Y	Y	Zr	Zr	0.21	0.11
	R4-3	Y	Y	Zr	Y	Zr	Y	0.40	0.40
	R4-4	Y	Y	Y	Zr	Zr	Y	0.30	0.30
	R4-5	Zr	Y	Y	Y	Zr	Y	0.48	0.34
	R4-6	Zr	Y	Y	Y	Y	Zr	0.45	0.22
5	R5-1	Zr	Y	Y	Y	Y	Y	0.17	0.17
	R5-2	Y	Y	Y	Y	Zr	Y	0.54	0.34
6	R6-1	Y	Y	Y	Y	Y	Y	1.08	1.08

Table S3. The pseudocode for estimating proton site energies in a given supercell of Y-doped $BaZrO_3$, which are estimated from the energy differences between adjacent sites depending only on the local Y configurations ($\Delta E_{i,j}$: site energy difference between sites i and j). However, the site energy is not uniquely determined due to slight inconsistency of $\Delta E_{i,j}$ between various local Y configurations, which is therefore estimated as the average value. n_{site} and n_{loop} denote the number of sites in the supercell and the number of loops, respectively. n_{loop} was here set to $n_{\mathrm{site}}/10$.

Algorithm: Site Energy Estimation ($\{\Delta E_{i,j}\}$, n_{site}, n_{loop})

Initialize:

Estimated site energy at site i in loop l: $E_i^{(l)} = \mathrm{nil}$ $(i = 1, 2, ..., n_{\mathrm{site}})$

for l **in** $1..n_{\mathrm{loop}}$ **do**

Initialize the set of unsampled sites: $S_{\mathrm{unsmp}} = \{1, 2, \ldots, n_{\mathrm{site}}\}$

Initialize the set of sampled sites: $S_{\mathrm{smp}} = \emptyset$

Randomly sample a starting point from S_{unsmp} (Starting site No.: i_0)

$E_{i_0}^{(l)} = 0$, $S_{\mathrm{smp}} \leftarrow S_{\mathrm{smp}} \cup \{i_0\}$, $S_{\mathrm{unsmp}} \leftarrow S_{\mathrm{unsmp}} \setminus \{i_0\}$

while $S_{\mathrm{unsmp}} \neq \emptyset$ **do**

Randomly sample an unsampled site adjacent to any sampled site

(Sampled site No.: i_{smp}, Adjacent site No.: i_{adj})

$E_{i_{\mathrm{smp}}}^{(l)} = E_{i_{\mathrm{adj}}}^{(l)} + \Delta E_{i_{\mathrm{adj}},i_{\mathrm{smp}}}$, $S_{\mathrm{smp}} \leftarrow S_{\mathrm{smp}} \cup \{i_{\mathrm{smp}}\}$, $S_{\mathrm{unsmp}} \leftarrow S_{\mathrm{unsmp}} \setminus \{i_{\mathrm{smp}}\}$

done

$E_{\max} = \max_i E_i^{(l)}$

for i **in** $1..n_{\mathrm{site}}$ **do**

$E_i^{(l)} = E_i^{(l)} - E_{\max}$

done

done

Output:

Averaged site energy at site i $(i = 1, 2, ..., n_{\mathrm{site}})$: $E_i^{\mathrm{ave}} = \frac{1}{n_{\mathrm{loop}}} \Sigma_l E_i^{(l)}$

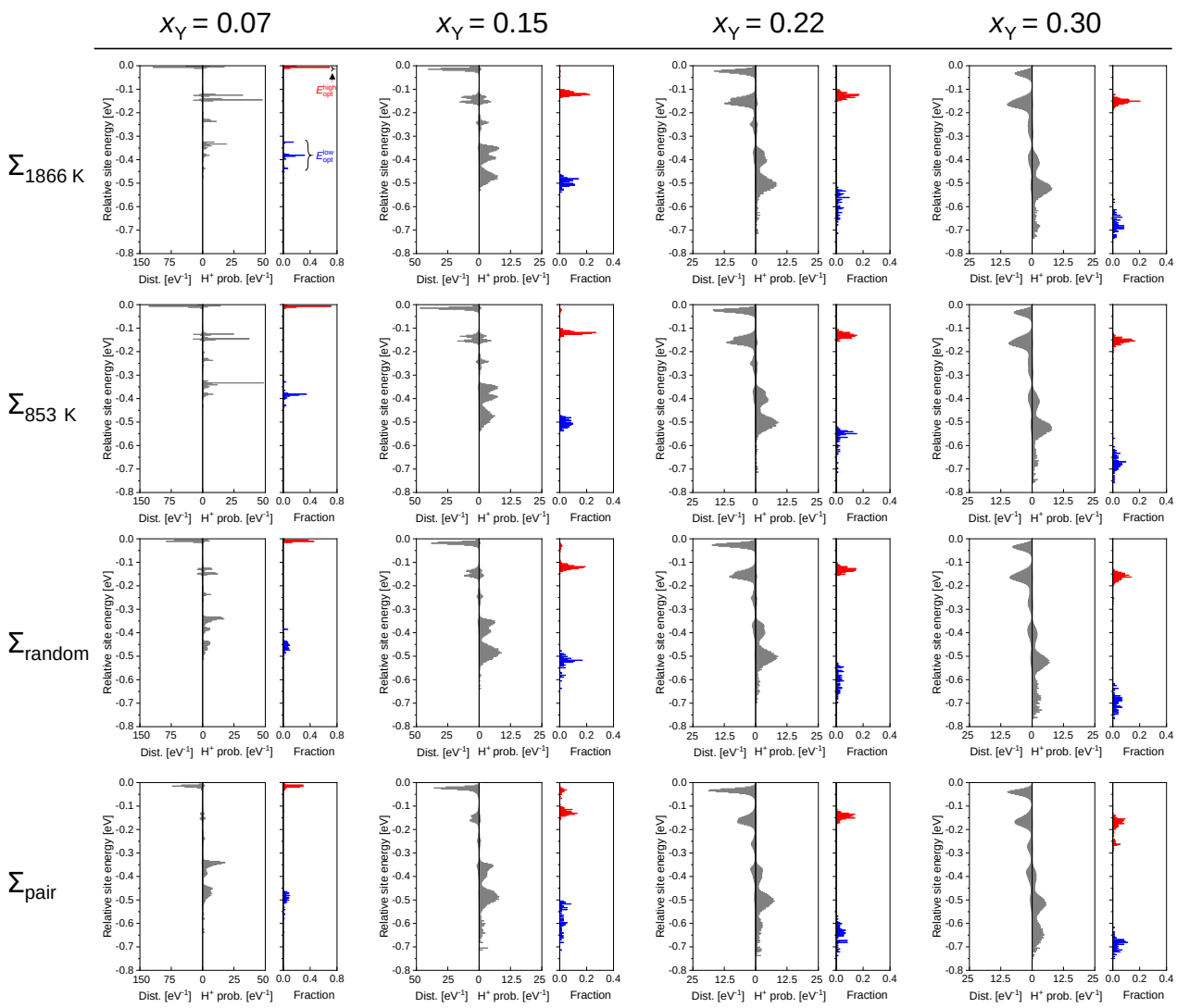

Figure S3. The normalized site-energy distributions (Dist.) in the 72 supercells at various Y concentrations and in various Y configurations (Σ_{1866K}, Σ_{853K}, Σ_{random}, and Σ_{pair}). The proton existence probability at 600 K (H^+ prob.) is also shown in each figure. The normalized histograms of the lowest and highest site energies along the optimal paths are shown on the right side by the blue and red bars, respectively.

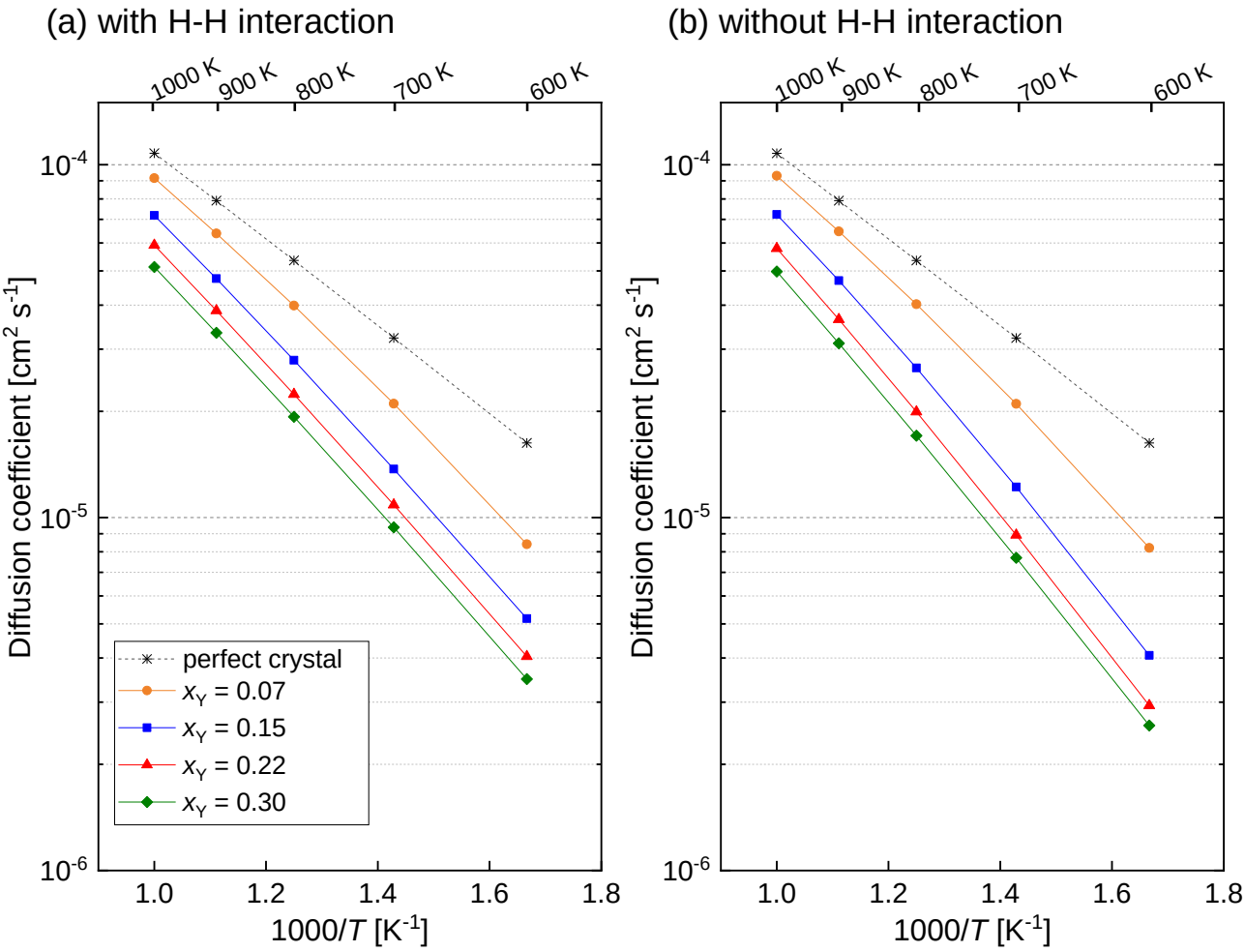

Figure S4. The calculated proton diffusion coefficients as a function of inverse temperature in the case of Σ_{1866K} configuration of Y dopants. Figures (a) and (b) show the proton diffusion coefficients with and without the proton-proton interactions, respectively. The site occupancies of Y dopants on the Zr sites, x_Y, are 0.07, 0.15, 0.22, and 0.3. The black broken lines show the proton diffusion coefficients in the perfect crystal with neither H-H nor Y-H interaction for reference.